# Title: High Temperature Lithium Corrosion of Fusion-grade Structural Steels

**Authors: Bradley A. Young[1,2,*], Junliang Liu[1,3], Dirk Honecker[4], Stephen King[4], Thomas P. Davis[2,5], David E.J Armstrong[1]**

[1] Department of Materials, University of Oxford, Parks Road OX1 3PH UK

[2] Oxford Sigma, Oxford Centre for Innovation, New Road, Oxford, OX1 1BY, UK

[3] Department of Nuclear Engineering and Engineering Physics, University of Wisconsin–Madison, 1500 Engineering Drive, Madison, WI 53706, USA.

[4] ISIS Neutron and Muon Source, Science & Technology Facilities Council, Rutherford Appleton Laboratory, Harwell Campus, Didcot, OX11 0QX, UK

[5] Nuclear Futures Institute, Bangor University, Bangor, LL57 1UT, UK

* bradley.young@st-annes.ox.ac.uk; bradley.young@oxfordsigma.com

## Abstract

Fusion energy has the promise to provide a carbon-free, near-unlimited energy source for the future. An essential component of a fusion power plant is the breeder blanket which must produce tritium via the transmutation of lithium into tritium via neutron capture. A pure liquid lithium-based blanket design has shown promise in performance of tritium breeding, cooling, and lack of requirement for isotope enrichment [1]. How the liquid lithium interacts with and degrades the mechanical performance of the breeder blanket components will largely determine the success of commercial fusion powerplants. High temperature (>450 °C) liquid lithium corrosion of "fusion-grade" materials is not well known and must demonstrate suitable resistance to provide confidence in their performance during service. This study develops a method for exposing candidate materials to pure liquid lithium for extended periods at relevant temperatures, and subsequent analysis of corroded samples is performed. The corrosion resistance of fusion-relevant steels including EUROFER ferritic-martensitic steel, Castable Nanostructured Alloy (CNA), and 14YWT Oxide-Dispersion Strengthened steel at 500 °C for 24 hours was analysed using advanced characterisation techniques including electron microscopy and small-angle neutron scattering (SANS). It was found that significant corrosion occurs on all these materials. For CNA, significant loss of nanosized particles, such as carbides, was observed by SANS. For 14YWT, the Y-Ti-O particles show stability under exposure to liquid lithium. The results indicate that these fusion-grade steels are unlikely to possess sufficient corrosion resistance for application in a liquid lithium breeder blanket at this temperature regime without any form of protection. Nevertheless, the inclusion of relatively thermodynamically stable nano-oxides within the microstructure may be a promising strengthening mechanism compatible with the environment.

## 1. Introduction

Fusion energy could become the ultimate terrestrial energy source for the future because it promises to have near-limitless fuel supply [2], release no carbon emissions at source, and provide the energy demand that could lift the world out of energy poverty [3]. The main fuel type pursued by fusion technology is the deuterium-tritium (D-T) fuel cycle [4]. The supply of tritium must be bred within the reactor as its half-life of 12.3 years means there is limited natural abundance [2]. Tritium production can be achieved by the transmutation of lithium to tritium and helium by incident neutrons which are a product of the fusion D-T reaction. A particularly attractive engineering method to achieve this is the use of flowing – natural or Li-6 enriched isotope mixture – liquid lithium within the breeder blanket due to the high atomic density of lithium [5]. The application of flowing liquid lithium as a dual-purpose breeder-coolant in the breeder blanket section of a fusion reactor in the temperature range of 500-700 °C

[6] is an attractive design concept to fulfil the needs of the fusion power plant. The structural materials proposed must have suitable resistance to extreme environments and any degradation mechanisms must be suitably understood to provide confidence in their performance during service. Reliable data on the corrosion resistance of proposed structural materials in liquid lithium over this temperature range is scarce. In 2024, at least 24 organisations pursuing fusion technology have expressed the desire to include liquid lithium as part of their concepts [7], [8]. However, using liquid lithium for this application presents significant technical challenges due to lithium's corrosive properties at the expected operation temperature of the breeder blanket component: at or in excess of 500 °C.

Steels have widely been considered as the primary choice of structural material for breeder blankets in fusion due to the relatively extensive knowledge of their properties under the temperature and irradiation environment and the widespread experience of construction using them [9], [10], [11]. Specific reduced-activation ferritic-martensitic (RAFM) fusion-grade steels, such as EUROFER [12], Oxide Dispersion Strengthened steels [9], and Castable Nanostructured Alloys (CNA) [13] have been designed specifically for fusion components, such as breeder blankets.

The corrosion properties of liquid lithium have been studied since the 1950s due to interest in its use a coolant for nuclear reactors [14]. Significant research output was produced from then until the mid-1980s which focused on understanding of potential corrosion mechanisms and preliminary assessments of corrosion resistance of certain materials [15], [16], [17], [18], [19]. Identified mechanisms from this research included simple dissolution of material elements that were soluble in lithium as well as mechanisms involving reactions of interstitial elements (including carbon, nitrogen, and oxygen which may come from the material or lithium impurities) with lithium to remove material from the samples. The phenomenon of thermal gradient mass transfer means that these mechanisms would not be halted due to lithium saturation in-service as material removed by corrosion is continually redeposited elsewhere in the system in a flowing loop [15], [19]. Reactions between interstitial elements and lithium has led to carbides in steels being shown to be particularly vulnerable to corrosive attack and grain boundary penetration being observed due to the increased concentration at grain boundaries of interstitial elements and other elements which may be more soluble in lithium [15], [17], [18], [19]. The preferential removal of certain elements due to interstitial reactions or increased solubility can result in phase changes where particular elements are key to phase stabilisation [17], [19]. Whilst steels were often studied, these did not include any "fusion-grade" materials. Furthermore, limitations of characterisation techniques of the time present an opportunity to understand the corrosion mechanisms better for recently developed fusion materials. In 1989, Bell et al. investigated corrosion of 12Cr-1MoVW (such as HT9) steels at up to 580 °C [20]. This study in a thermal convection system found a strong dependence of corrosion on surface reactions involving carbon and nitrogen with precipitates in the steel at 500 °C. A 'pebbled' material surface following corrosion was observed, along with facetted 'nodules' on the surface. This is the most relevant research to the study presented here due to the similar material composition and relevant temperature regime.

To the authors' knowledge, there have been few publications on direct lithium corrosion at high temperatures (>450 °C) published in the scientific literature. Since the mid-2010s, there has been renewed interest in the corrosion of liquid lithium in fusion applications mainly for the breeder blanket component. Along with this component, lithium is also considered for plasma-facing components where liquid lithium flows over a first-wall structure [21], [22], [23] and as a fusion neutron source for materials testing [24]. These two alternative applications necessitate temperatures in the range of 300 °C as opposed to temperatures predicted in excess of 500 °C for breeder blanket components [25], [26]. As a result, there has been significant research performed in the lower temperature regime [16], [27], [28], [29], [30], for which the results are not applicable to assess compatibility in the breeder blanket temperature regime, as corrosion due to dissolution will depend strongly on temperature.

In this study, a variety of steels (EUROFER, ODS 14YWT, and CNA), which are of interest to the fusion community, have been exposed to static liquid lithium corrosion at 500 °C for 24 hours. No previous studies have been identified which analyse the corrosion resistance in lithium of any of these materials. The microstructural evolutions resulting from this exposure were examined using a combination of electron microscopy and small-angle neutron scattering. Discussions of corrosion mechanisms displayed by these materials and their potential suitability in a liquid lithium environment are also given.

## 2. Experimental Method

### 2.1. Materials

Samples of four types of steels which are relevant to the fusion industry were procured and prepared for liquid lithium corrosion testing.

Material 1: EUROFER is the European RAFM steel candidate material for fusion applications and is the structural material for the ITER Tritium Blanket Modules [12], [31], [32]. This sample was produced from a batch produced by Bohler Edelstahl GmbH in Austria which was then normalised at 980 °C for 0.5 hours and tempered at 760 °C for 1.5 hours followed by air cooling. The nominal composition of the material is approximately Fe-8.89Cr-1.11W-0.44Mn-0.19V-0.14Ta-0.06Si-0.12C-0.01N in weight percent. Microstructural characterisation, mechanical testing results and the nominal compositional range of this EURORER batch has been thoroughly analysed and can be found in reference [33].

Material 2: CNA was produced by Oak Ridge National Laboratory (ORNL). The measured chemical composition of the received sample, as measured by X-ray Fluorescence analysis was Fe-8.77Cr-0.57Mn-1.46W-0.1Si-0.13Ti-0.08V-0.05Ta-0.09C and originated from heat number FTT1 of the GAMOW heat. Following the melt, the metal was subjected to homogenisation at 1170 °C for 2 hours followed by a ~70% thickness reduction by hot rolling at 1150 °C; it was then normalised between 1150-1170 °C for 0.5 hours, water quenched, and tempered at 750 °C for 1 hour followed by air cooling. Previous studies on the microstructure, mechanical properties, and radiation resistance of this material can be found in references [13], [34].

Material 3: 14YWT ODS steel is a candidate structural material for a fusion breeder blanket due to its radiation damage tolerance, strength, and creep resistance [10], [35], [36]. These steels contain a high density (~$10^{23}$ $m^{-3}$) of nano-oxides of radius <2 nm [37]. The nano-oxide particles improve the strength and high-temperature creep resistance of the ferritic steel and act as effective sinks for the recombination of irradiation-induced defects [9]. 14YWT (nominal wt% composition: Fe-14Cr-3W-0.2Ti-0.25$Y_2O_3$) which includes Y-Ti-O as its nano-oxide particles, was obtained for research as part of this study. This material was manufactured at the University of Oxford using hot isostatic pressing (HIP) consolidation following mechanical milling of pre-alloyed powders. The manufacturing process is detailed in the appendix in Gorley [38] and its composition was measured by Davis et al. [10]. The microstructure of this steel has been previously extensively studied by Gorley, Burrows, Jones and Davis [33], [38], [39], [40].

Material 4: In order to be able to isolate the effects on corrosion resistance of the nano-oxide particles included in 14YWT, an equivalent non-ODS steel produced by Gorley using identical methods – 14WT (nominal wt% composition: Fe-14Cr-3W-0.2Ti) – was also studied and has been previously characterised by Gorley and Jones [33], [38] and its composition was measured by Jones [33].

Samples were produced of all steels from the received material with dimensions of approximately 15 x 10 x 1 mm with a small hole drilled near one of the short edges so that they could be hung by tungsten wire for suspension within the liquid lithium. The faces of the samples were finished with either a final stage of 1 μm diamond suspension polish (for the EUROFER sample) or a colloidal silica suspension polish (for the CNA, 14WT, and 14YWT samples) to provide a flat surface morphology before exposure which is relatively consistent across all the samples tested.

### 2.2. Corrosion method

Immersion tests in static liquid lithium were performed on samples indicated above. For the corrosion tests, approximately 1.5 g of 99.9% purity lithium obtained in ribbon format from Sigma-Aldrich was contained within a crucible of molybdenum foil and covered with a stainless-steel lid. This method has previously been used to investigate the lithium corrosion of $SiC_f$/SiC composites [41]. The solid lithium in the crucible was first introduced to a pre-heated furnace at 500 °C to melt and homogenise for approximately one hour. The furnace was housed in an MBraun MB200B glovebox which maintained an argon inert gas atmosphere with controlled and monitored oxygen and moisture levels. The crucible was the briefly removed from the furnace and the hanging steel sample was then positioned to be approximately half-submerged in the liquid lithium pool before returning the crucible to the furnace. During the 24-hour corrosion testing, the system was remotely monitored for safety purposes and the temperature was maintained at 500 °C (±0.5 °C); the $O_2$ and $H_2O$ levels were both maintained below 0.1 ppm. At the end of the exposure period, the crucible was removed from the furnace at temperature and the sample lifted out of the liquid lithium using the tungsten wire. The sample was allowed to cool whilst suspended at room temperature in the glovebox atmosphere to prevent adherence of the sample to other surfaces. Monitoring of nitrogen levels in the lithium liquid or the glovebox was not conducted due to the lack of capability.

### 2.3. Cleaning method

Following the cooling process, a thin layer of adhered lithium remained on the surface of the samples which were submerged during testing. To remove this layer, a solution of 95 vol% ethanol and 5 vol% water was prepared within a fume hood and the cooled samples were quickly transferred to separate beakers containing this solution within a few seconds of being removed from the glovebox. The samples were kept in the solution overnight to fully remove the adhered lithium. This solution is designed to react with any residual lithium on the sample surface so that the underlying sample surface can be observed. The reaction between water and lithium is quite aggressive and therefore ethanol was included in the solution to supress the reaction. This ensured the effervescence of evolved hydrogen was not vigorous and there was no noticeable increase in temperature of the solution. It is thought that the presence of this relatively mild solution, other than removing the adhered lithium, did not alter the surface morphology of the corroded samples. Therefore, any observed morphology is the result solely of changes caused by the corrosion testing.

### 2.4. Analysis methods

Samples were weighed before and after corrosion (after removing residual lithium as described above in the previous section) using a Sartorius Cubis® Ultra-Micro Balance with a readability of 0.001 mg. Each mass measurement was repeated at least three times with strong agreement between the results such that masses may be reported to the nearest 0.01 mg with certainty. It is thought that the mass loss experienced by a sample during corrosion is strongly dependent on the surface area exposed to the corrosive liquid. Therefore, the reported mass change results will be presented in the format of a mass change per exposed surface area ($mg/cm^2$). After exposure, the submerged area exhibited a different surface morphology and contrast compared to the unsubmerged area, aiding in the accurate measurement of the exposed surface area of the sample. It is assumed that no significant mass change occurs in the unsubmerged portion of the sample and therefore that any mass change resulting from the sample is overwhelmingly concentrated in the portion of the sample which was submerged in the liquid lithium.

Secondary electron (SE) and backscattered electron (BSE) imaging were carried out on Zeiss Crossbeam 540 and Tescan Mira 3 scanning electron microscopes (SEM), both equipped with field emission sources. The SEM micrographs can reveal surface microstructural changes, indicate elemental

distribution within the microstructure, and give insights into the mechanisms and extent of corrosion in each sample.

Small Angle Neutron Scattering (SANS) experiments were conducted on the Sans2d instrument which is part of the ISIS Neutron and Muon Source (www.isis.stfc.ac.uk) and used to determine the presence of features within the microstructure of the tested materials at specific length scales. This can be achieved as the scattering vector, $Q$, of the diffracted neutrons is inversely proportional to the characteristic length scale, $d$, of the microstructural feature which has caused the scattering as shown in Equation 1 [42].

$$d = {}^{2\pi}/_{Q} \qquad (1)$$

where

$$Q = {}^{4\pi}/_{\lambda} \cdot sin(\psi) \qquad (2)$$

λ is the neutron wavelength and 2ψ is the scattering angle. For these experiments, flat samples were prepared measuring approximately 1.5 x 1.5 cm and were thinned to have a thickness of approximately 0.6 mm in order that they would be sufficiently transparent to neutrons and could be easily loaded into the sample holders of the available equipment. As thin samples were necessary for this transmission analysis technique, corroded samples were thinned to approximately half of their original thickness, therefore only one of the surfaces of the analysed sample was exposed to lithium in the corrosion test. The thickness of each sample was measured to an accuracy of 0.01 mm and an average of at least eight measurements was collected. These measurements resulted in a maximum of 4% error in the measured thickness of a sample and the SANS data have been normalised to account for the variation in thickness of different samples. SANS data were collected in two measurement sessions using a more restricted wavelength range of 4.3 – 11 Å than would be normal to avoid a Bragg edge at shorter wavelengths and mitigate multiple scattering effects at longer wavelengths. The two, two-dimensional, position-sensitive detectors were situated at either 2.4 and 4 m (giving $0.004 < Q\ (Å^{-1}) < 0.84$) or 4 and 8 m (giving $0.0024 < Q\ (Å^{-1}) < 0.48$) from the sample, respectively, offset slightly to either side of the transmitted beam, and the incident beam was collimated to 6 mm diameter. Scattering data were accumulated for 35 - 60 min/sample and transmission data for 7 - 10 min/sample. The raw detector data were azimuthally integrated, corrected, and merged using the Mantid framework (www.mantidproject.org, versions 6.7.0 and 6.9.0) following standard ISIS facility workflows. Results of the neutron scattering experiments are displayed as a comparison between two samples of the same material: one the as-received sample, and the other following corrosion in static liquid lithium at 500 °C for 24 hours (after removal of residual surface lithium using the cleaning method described above). This observation of this data enables comparison of the change in characteristic length scales from one to several tens of nm contained within the microstructure of a material before and after corrosion has occurred.

## 3. Results

### 3.1. Weight change

The mass change per surface area of exposure measurements are shown in Table 1 and have also been used along with an approximation of the densities of the material [43] to produce a value for volume change per surface area exposed for each sample. This measurement could be described as a value of thickness loss with the assumption of uniform surface removal because of corrosion. Further results shown below demonstrate that uniform surface removal is not observed.

*Table 1: Quantitative results of sample mass change due to corrosion. The calculated volume chamge assumes that the samples have a density equivalent to iron, 7.87 g.cm$^{-3}$ [43]*

| Sample | EUROFER | CNA | 14YWT | 14WT |
|---|---|---|---|---|
| Measured mass change per surface area exposed (mg.cm$^{-2}$) | -0.06 | -30.52 | +0.01 | +0.03 |
| Calculated volume change per surface area exposed (μm$^3$.μm$^{-2}$) | -0.076 | -3.878 | +0.013 | +0.038 |

### 3.2. **Microscopy and SANS**

For EUROFER, Figure 1 shows the surface morphology of sample following exposure to static liquid lithium for 24 hours at 500 °C. Two distinct regions of surface morphology variation can be seen in Figure 1(a), consisting of roughly circular regions and second regions between these which appear to be more severely affected. Figure 1(b) shows a higher magnification image of one of the second, more severely affected, regions where a dendritic-like structure with individual holes can be observed. The EUROFER sample used in this study is the same, and was prepared in the same way, as the material analysed by Jones [33] without corrosive effects.

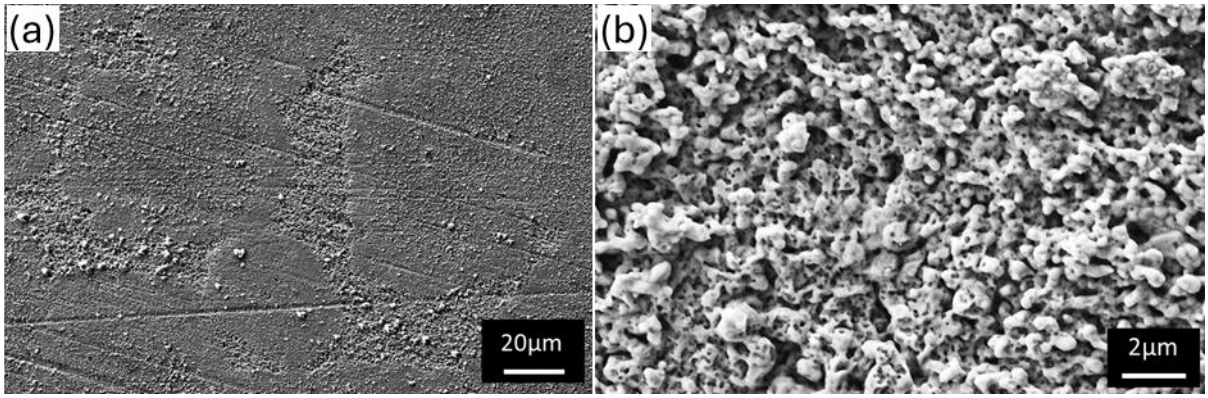


*Figure 1: SE micrographs showing the surface of a EUROFER sample which was polished and then submerged in molten lithium at 500 °C for 24 hours, residual lithium adhered to the surface was removed before imaging.*

For CNA, Figure 2 (a) and (b) show secondary electron (SE) micrographs of the same region of the same sample before (a) and after (b) the 24-hour exposure to 500 °C liquid lithium. Figure 2(c) shows a higher magnification SE micrograph of the sample after corrosion. The contrast in the SE imaging is predominantly a result of surface topology. In Figure 2(a) the surface relief which can be seen is caused by slight variation in the heights of some grains due to the colloidal silica polishing technique which allows the grain structure to be seen in some sections. The surface relief visible in Figure 2(b) is caused by non-uniform surface corrosion. In some regions of Figure 2(a) and (b), the same grains may be identified before and after corrosion.

Figure 2(c) shows a higher magnification secondary electron image of the corroded CNA sample which confirms the crevassing caused by preferential corrosion along the lines of grain boundaries. Also evident in the image in Figure 2(c), especially clearly in the grain in the bottom-left, is the presence of non-uniform surface topology and terracing which varies in appearance between different grains.

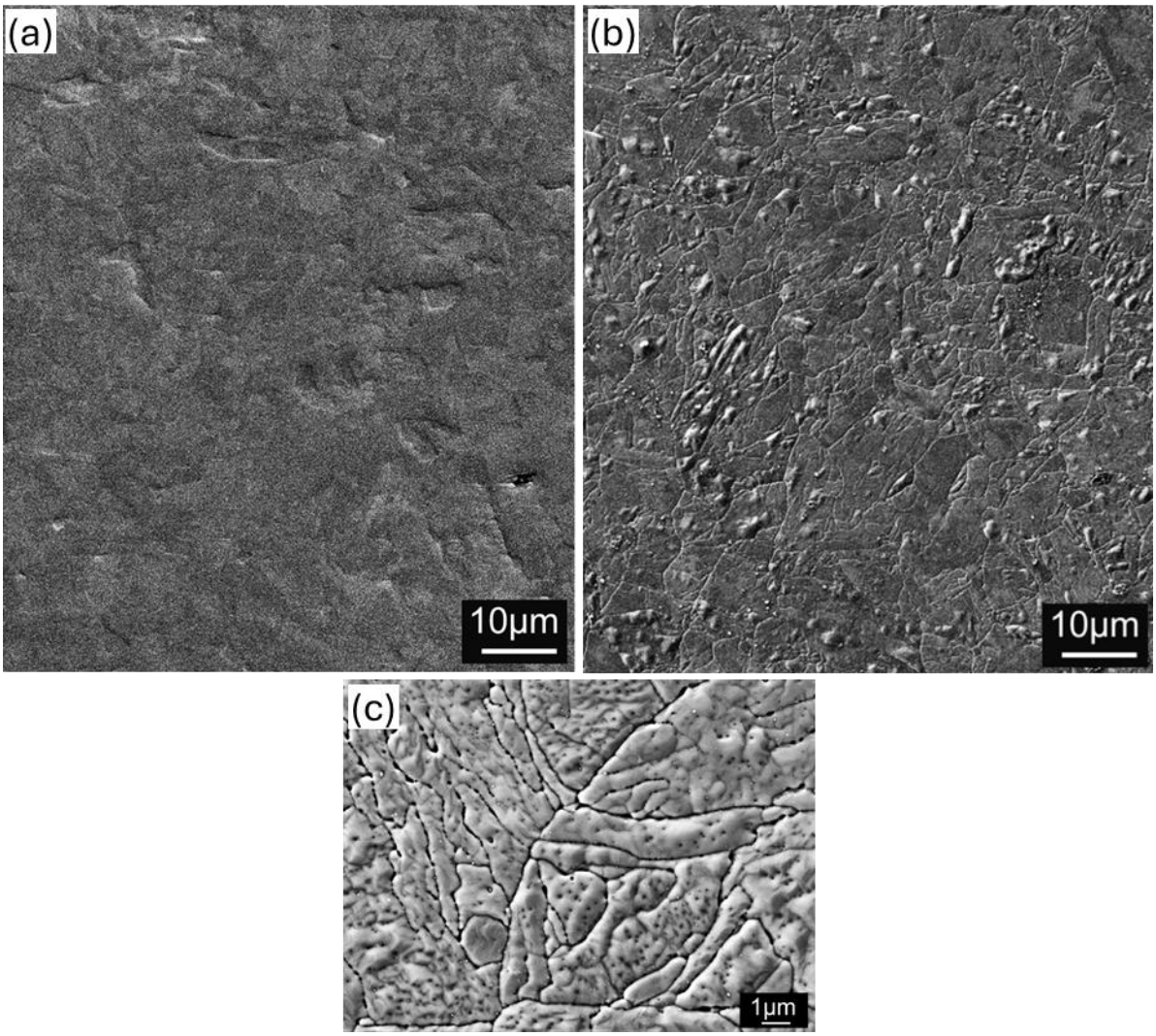


*Figure 2: SE micrographs showing the surface of a polished CNA sample (a) before submersion and (b,c) after submersion in molten lithium at 500 °C for 24 hours, residual lithium adhered to the surface was removed before imaging. (a) and (b) show the same region of the sample before and after corrosion respectively.*

The SANS data for CNA is shown in Figure 3. For the uncorroded CNA sample (shown by the purple line in Figure 3(a)), a notable increase in normalised scattering intensity from the smooth curved shape can be seen between Q values of approximately 0.2-0.6 $Å^{-1}$ as indicated by the shaded region in the figure. Scattering vector values are inversely proportional to the length scale of the microstructural features which cause the scattering event as shown in Eq. 1. Using this relationship, the Q values indicated in the figure of 0.2-0.6 $Å^{-1}$ correspond to a characteristic microstructural length scale of 1-3 nm. Therefore, this data confirms the presence of the nano-carbides in the as-received sample. At lower Q the data is dominated by a $\sim Q^{-4}$ contribution indicative of well-defined interfaces at longer length scales.

In the data presented for the sample following corrosion (shown by the green line in Figure 3(a)), the same region appears flatter. This is supported by Figure 3(b) which shows the ratio of the scattering intensities between the two samples where there is a noticeable decrease in ratio in the identified region, corresponding to the same 1-3 nm length scale as indicated in Figure 3(a).

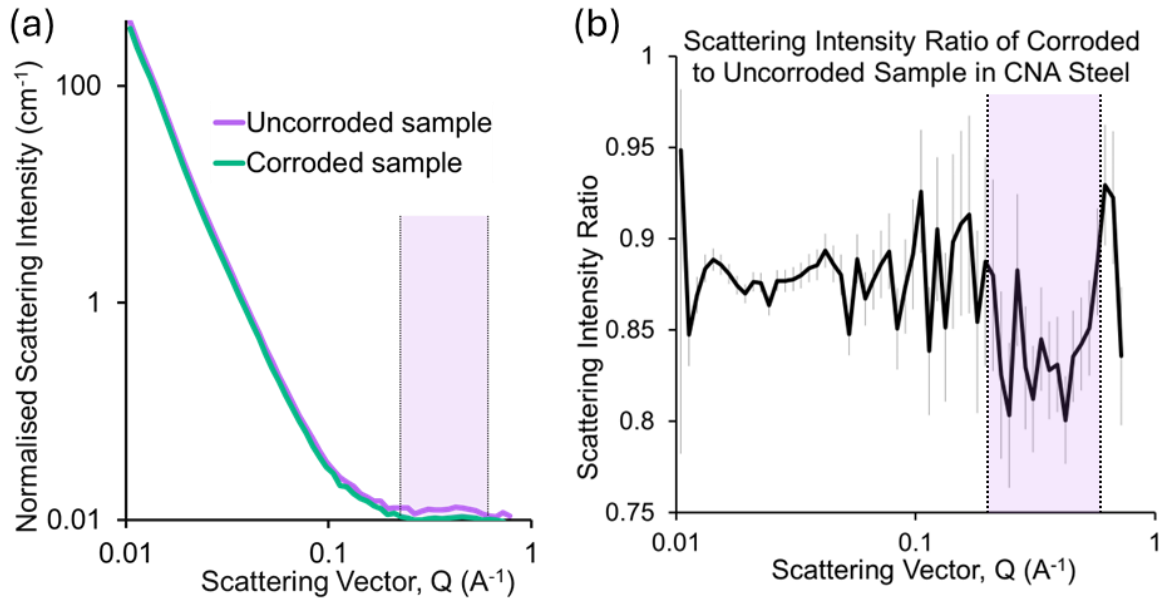


*Figure 3: SANS results for the CNA material, uncorroded and corroded by molten lithium at 500 °C for 24 hours (residual lithium adhered to the surface was removed before analysis). (a) shows the variation of scattering intensity with scattering vector for both samples, corrected for the specific sample thickness, and (b) shows the ratio between the measured intensities of the two samples.*

For 14WT steel, Figure 4Figure 5(a) shows a backscattered electron micrograph of the uncorroded material sample, in which the differences in average atomic number of the elements in the phase contribute strongly to the contrast shown in the image. The grain structure of the material can also be seen by the contrast caused by the variation in crystal orientation. Darker spots throughout the image indicate the titanium oxides which are known to be present in the sample and the bright regions on the boundary between grains represents a tungsten, chromium, and carbon enriched intergranular phase [33], [38]. The remainder of the grain boundary regions which are not occupied by this phase are enriched in titanium because of elemental segregation [38]. In Figure 4(b), SE micrographs of the corroded 14WT sample are show in which the contrast is more strongly affected by the surface topology of the sample.

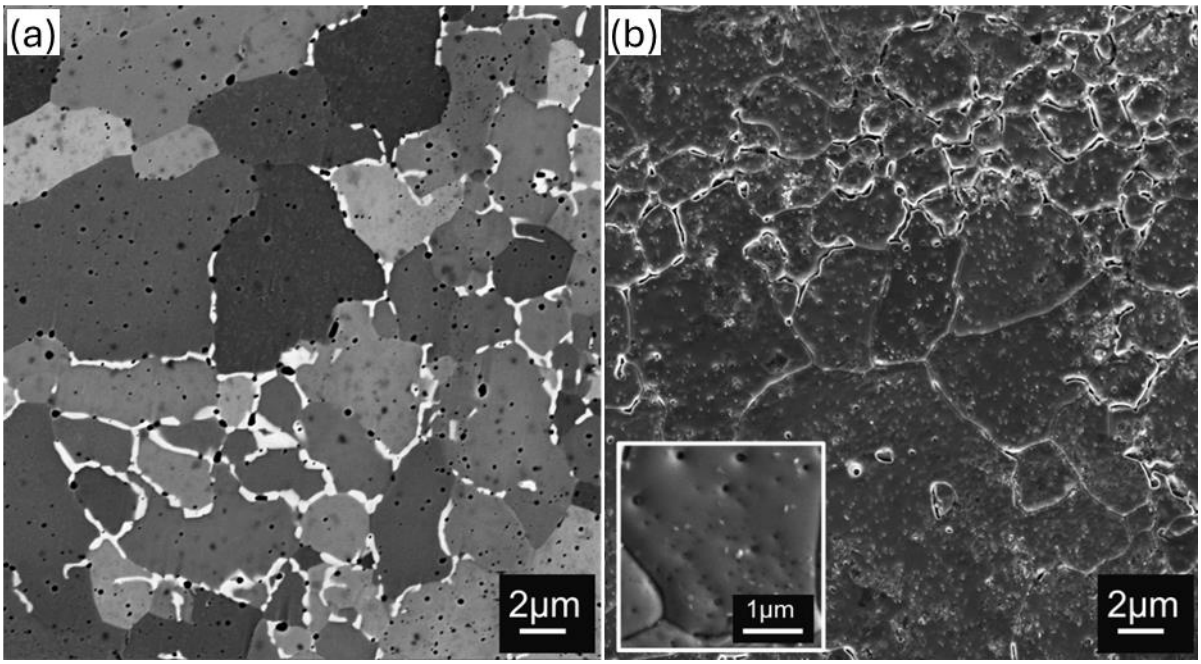


*Figure 4: (a) Backscattered and (b) SE micrographs of a polished sample of 14WT steel material (a) before submersion and (b) after submersion in molten lithium at 500 °C for 24 hours, residual lithium adhered to the surface was removed before imaging. Inset in (b) is a higher magnification image of a region near the centre of (b).*

For ODS 14YWT steel, the pre- and post-corrosion micrographs are found in Figure 5. Figure 5(b)&(c) show the surface of 14YWT ODS steel following the corrosion exposure, where the bright, facetted, surface particles are immediately observable. The identity and the cause of the presence of particles such as these has been discussed previously in this work and in references [10], [33], [38]. Additionally in Figure 5(b)&(c), crevassing at grain boundaries is observed following corrosion, as was similarly observed in Figure 2(b)&(c) and Figure 4(b).

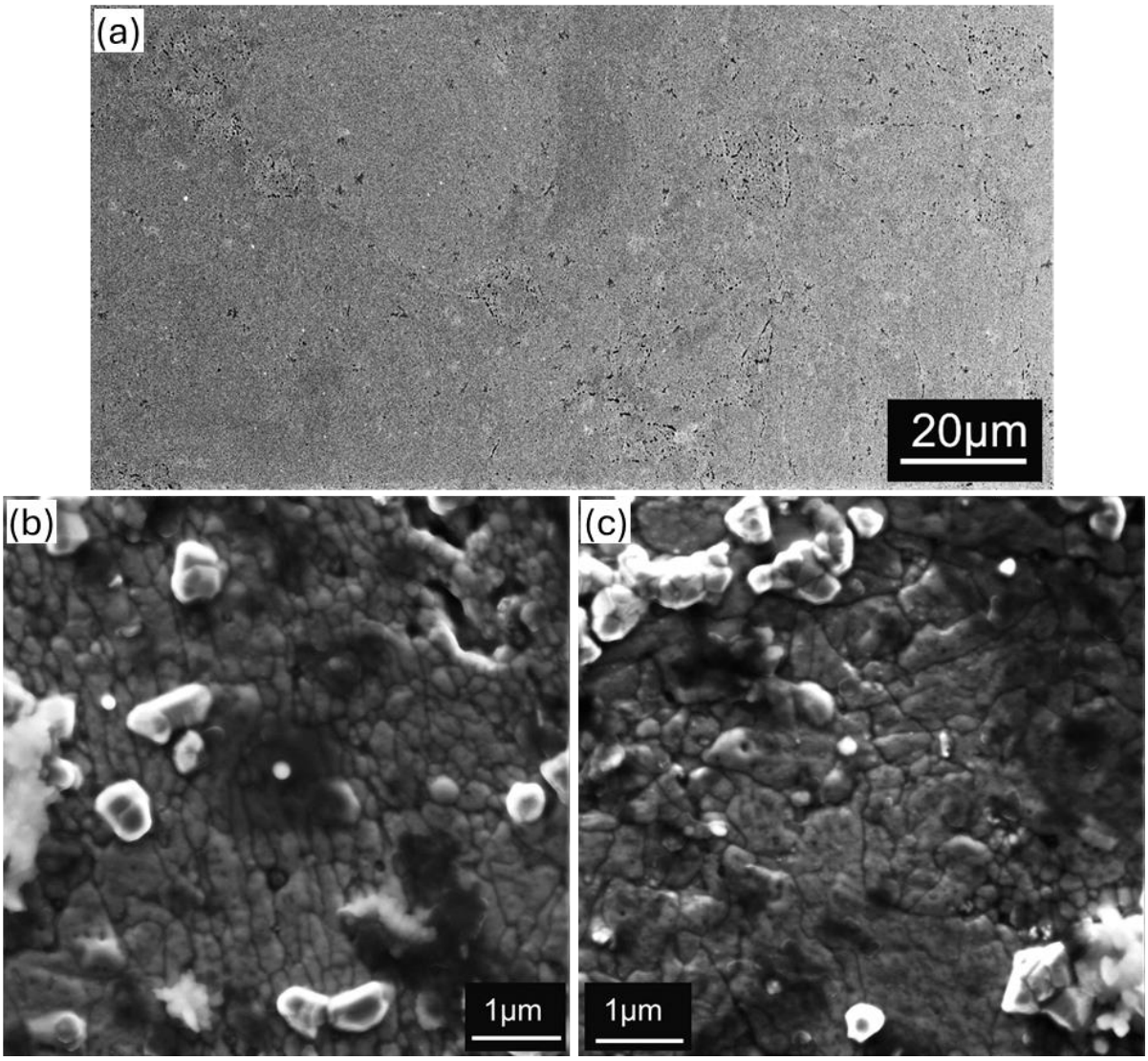


*Figure 5: SE micrographs of a polished sample of 14YWT ODS steel material (a) before submersion and (b,c) after submersion in molten lithium at 500 °C for 24 hours, residual lithium adhered to the surface was removed before imaging.*

The effects of corrosion on the nanoscale oxides could not be directly resolved by the SEM imaging due to the limited spatial resolution. Therefore, as was investigated for the CNA material, samples of the 14YWT material before and after corrosion were analysed using the SANS technique and the results of this are shown in Figure 6. In Figure 6(a,b) the shaded region highlights scattering vectors (0.21-0.5 $Å^{-1}$) which correspond to the length scale (1.2-3 nm) over which nano oxides occur [10]. Figure 6(b) shows the ratio of measured scattering intensity between the two samples and within the highlighted region the ratio of scattering intensities between the samples is approximately 1. The scattering intensity ratio rises significantly above 1 between scattering vectors of 0.0024-0.12 $Å^{-1}$.

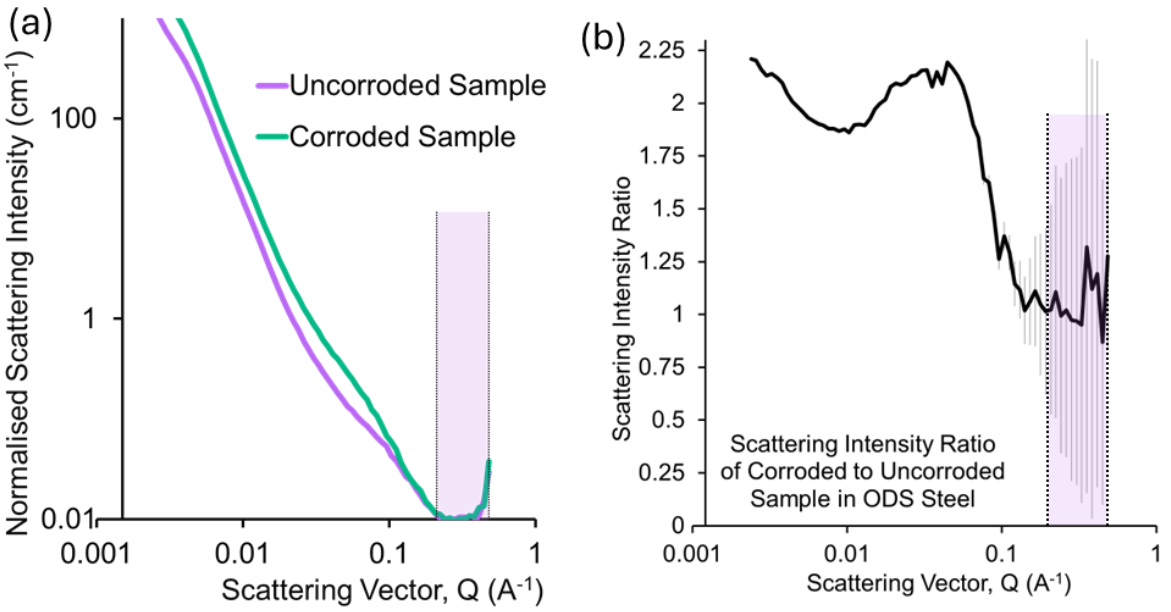


*Figure 6: SANS results for the 14YWT ODS steel material, uncorroded and corroded in molten lithium at 500 °C for 24 hours (residual lithium adhered to the surface was removed before analysis). (a) shows the variation of scattering intensity with scattering vector for both samples, corrected for the specific sample thickness, and (b) shows the ratio between the measured intensities of the two samples.*

## 4. Discussion

### 4.1. Mass changes

The measurement of weight changes shown in Table 1 can begin to give an idea of the level of corrosion that has occurred on a sample. The observation of measured mass gain of some samples following exposure to the corrosive liquid is unexpected as material removal would be expected to dominate. However, measurement repeats have confirmed this result. A possible explanation is the addition of weight to the sample due to corrosion products being deposited on the surface, as may be observed especially in Figure 1(a) and Figure 5(b,c). A measured weight gain as a result, correlated with the observation of surface products forming on the sample, has also been reported by Bell et al. [20]. Characterisation techniques available were not able to identify the chemistry or crystal structure of surface particles which would aid in identification of their origin. A plausible explanation of the surface particles is Li-Cr-O compounds analogous to those observed in corrosion of steels in liquid sodium [44].

Whilst mass change measurements can provide useful and easy comparisons between samples, this method is unable to reveal insight into the corrosion effects on a material. This is because the method assumes that all effects result in a mass loss and that the loss of mass is the major negative factor for the in-service performance of the material. Further microstructural analysis will be presented which indicates that material loss occurs in a highly non-uniform manner and that there are other microstructural alterations which are likely to be more significant for the material behaviour than the uniform removal of surface material.

### 4.2. EUROFER

The porous structure identified in the microstructure of the corroded EUROFER in Figure 1(b) indicates that corrosion may be enhanced at, and around, sites of preferential attack caused by more susceptible microstructural features. An example of this is likely to be the presence of Ta-rich or V-rich MX carbides

and Cr-rich $M_{23}C_6$ carbides which are common in the microstructure of Eurofer and have a characteristic size of 8-40 nm and 25-200 nm respectively [45]. This analysis would result in a significant removal of material in areas such as the one shown in Figure 1(b).

The cause of the two distinct regions identified in Figure 1(a) is unclear, especially given that the characteristic length scale of the roughly circular regions does not correspond to the size of the grains in the microstructure identified by Jones via electron backscatter diffraction (EBSD) analysis in which the diameter of grains with approximately equiaxed morphology is generally no larger than 10 μm [33]. Also visible in Figure 1(a) is the presence of particles which are raised from the surface of the sample; these appear bright in the image and are highly facetted. As discussed in the previous section, these particles are identified as corrosion products by comparison with similar results reported in the literature [20], [44], although the analysis performed has been unable to identify their nature. An overall loss of mass is measured in the sample despite the existence of these additional particles.

### 4.3. CNA

This direct comparison between Figure 2 (a) and (b) confirms that the overall grain structure of the material has remained and gives strong evidence of preferential material removal at grain boundaries. Enhanced corrosion at grain boundaries is caused by the increased free energy of the interface in these regions and segregation of solute elements to the boundaries which are more susceptible to dissolution in the lithium. The effect of this on in-service components, which will be subjected to a load, is to produce surface stress concentrations which will increase the likelihood of failure of the component. This effect is likely to greatly increase the impact of corrosion on the material's performance compared with the uniform surface removal of material.

The terracing observed in Figure 2(c) is a result of the dissolution of material from the surface of the sample with a dependency on crystallographic orientation. This phenomenon has previously been observed in corrosion tests with other fluids [46].

Intragranular circular regions of enhanced corrosion which appear as black dots in the image are also visible in Figure 2(c). It is known that the microstructure of this CNA sample contains nanoscale intragranular carbides [13] and this observation of corrosion surface morphology is suggestive of the fact that the preferential dissolution of these particles leads to these circular pits. Confirmation of this via direct observation of the precipitates before and after corrosion is not possible using SEM analysis. SANS can identify the presence of nano-sized particles in the material. A comparison of neutron scattering results between the uncorroded and corroded CNA material has been performed and is shown in Figure 3.

Observation of the data within the shaded regions of Figure 3 confirms the theory that the nanoscale intragranular carbides are preferentially removed from the microstructure during the corrosion process.

Another notable feature of the data in Figure 3(a) is that the line representing data from the corroded sample is consistently beneath that of the uncorroded specimen. Figure 3(b) confirms this observation by showing that the ratio of scattering intensity between the two samples is consistently around a value of 0.88. This would indicate that the corroded sample also has an overall measurably lower density of microstructural features in the 3-63 nm length scale range than the uncorroded sample which suggests that material other than only the nano-carbides have been removed during corrosion. This is consistent with the high measured mass loss shown in Table 1.

Given that a homogenous distribution of the carbides throughout the material is expected, the scale of the sample on which these observations occur is notable as SANS is a transmission-based technique which shows results based on the entire thickness of the sample. In this case, the corroded sample analysed was approximately 0.7 mm thick and only one of its two faces was directly exposed to the corrosive fluid. Although only the sample surface has been directly imaged, this would suggest that the

corrosion environment has a measurable effect at a relatively substantial depth into the surface of the steel for the effects to be observable by the SANS technique.

### 4.4. 14WT

For 14WT (the non-oxide-dispersion-strengthened steel variant), preferential corrosion effects at the grain boundaries is evident in Figure 4(b) which could be predicted given the segregation of titanium to grain boundaries in this material and the susceptibility of other materials to this effect, such as the CNA shown in Figure 2. It is also evident in Figure 4(b) that some intergranular regions are much more significantly affected than others. This is caused by the removal of the tungsten, chromium, and carbon enriched intergranular phase identified in Figure 4(a) and results in regions on the surface where significant amounts of removal of material can be observed. Other intragranular regions of preferential material removal are also visible, especially in the inset of Figure 4(b). The size and distribution of these regions, which appear as small holes, closely mirrors the distribution of titanium oxide precipitates identified in Figure 4(a) before corrosion. It is therefore likely that the titanium oxide precipitates are preferentially removed from the microstructure during the corrosion process.

Despite these identified regions where it is evident that material has been removed from the sample, a positive change in mass of the sample was measured as a result of the corrosion process as shown in Table 1. This is an unexpected result which appears to contradict the microscopy observations. A potential explanation is that there are corrosion products produced during the experiment which are then redeposited on to the surface of the sample meaning that the mass of the material removed from the microstructure remains on the sample as a compound with the addition of elements such as lithium, oxygen, and nitrogen. Evidence of this may be seen in the inset of Figure 4(b) where bright precipitates which are raised from the surface of the sample are visible. These bright spots can also be more widely observed across Figure 4(b). This finding indicates that the lack of mass loss during corrosion is not a reliable indicator of a lack of corrosive effects within the structure of the material.

### 4.5. 14YWT ODS

For 14YWT ODS steel, the micrographs found in Figure 5 indicate that the bright, facetted, surface particles exist extensively on the surface of this material following corrosion and these are thought to have the same origin as discussed for the similar particles on the 14WT material shown in Figure 4(b). This also correlates with the measurement of a mass increase of the sample following corrosion as shown in Table 1. It is surprising that the mass increase measured for this 14YWT sample is less than that measured for the 14WT sample despite the apparent appearance of more extensive surface particles in Figure 5(b)&(c) compared with Figure 4(b).

In addition, grain boundary crevassing is apparent in this material due to corrosion, as it was in the CNA and 14WT materials. The fine grain structure observable by this crevassing was also observed by Jones with electron backscatter diffraction (EBSD) analysis [33]. Whilst this is extensive due to the high density of grain boundaries, the severity of the effect at an individual boundary of 14YWT shown in Figure 5(b)&(c) appears to be less than that shown in Figure 4(b) for 14WT. The effect of elemental segregation to boundaries as a potential cause of preferential intragranular corrosion has been discussed previously in this work. This leads to a potential explanation for the reduced severity of intragranular corrosion in the 14YWT material compared with 14WT because the addition of $Y_2O_3$ precipitates to the microstructure would reduce the extent of oxygen segregation to the grain boundaries. Oxygen is an element which is known to increase the corrosion rate of materials in liquid metals [47] and the stabilisation of this element within a relatively thermodynamically stable compound such as $Y_2O_3$ is likely to reduce its deleterious effects on corrosion resistance of the 14YWT material. It has previously been shown in other materials that the chemical stability of precipitates within the microstructure containing interstitial elements such as nitrogen and oxygen can have a significant effect on the corrosion resistance of the material [48], [49].

Further visible in Figure 5(b), near the top right-hand corner of the micrograph, is an area where the material surface is no longer continuous, and a portion of the surface material appears to have been removed. One theory to explain this appearance is the possibility that a precipitate of a second phase such as titanium oxide was present in this part of the microstructure which has been preferentially removed. Whilst no precipitates have been identified within the microstructure which match the morphology of this hole exactly, the titanium oxide precipitates which have been identified are of approximately the correct size [33], [38]. Alternatively, significant corrosive attack of the grain boundaries could have resulted in the complete spallation of entire grains which then leads to increased exposure of adjacent grains leading to their accelerated subsequent spallation, resulting in the formation of the crevice which can be seen. Finally, it has been previously found by Gorley [33] and can be seen from the uncorroded micrograph in Figure 5(a) that residual porosity is evident due to a failure to fully consolidate the sample following powder processing. Therefore, it is possible that this area in Figure 5(b) is not caused by the corrosion process but rather residual effects left by the powder processing method.

The 14YWT SANS data, as shown in Figure 6., leads us to believe that there is no significant effect of preferential corrosion of the nano oxides in this sample and that in fact these precipitates are relatively resistant to corrosion. This is the opposite as was observed with respect to nano carbides within the CNA sample shown in Figure 3. Interpretation of this result suggests that the Y-Ti-O precipitates are relatively thermodynamically stable in comparison to the Li-O or any lithium-containing mixed oxides that could be formed.

Conversely, at scattering vectors between 0.0024-0.12 $Å^{-1}$ in Figure 6, a ratio between scattering intensity of the samples significantly above 1 can be seen. This suggests that there is an increased density of microstructural features with a length scale between 5-263 nm following the corrosion experiment. This observation suggests that the heat treatment associated with the corrosion exposure has caused further coarsening of the ODS steel, because during the manufacturing process of these samples optimised tempering processes was not performed (as provided by references [10], [38]). This hypothesis allows for the coarsening of titanium oxides and/or chromium carbides (such as MX or $M_{23}C_6$ type precipitates, as discussed by Davis [40]) during the corrosion which then exist within the identified 5-263 nm length scale range in the sample. It was expected that the material would be microstructurally stable under the associated heat treatment conditions of the test, however these observations would suggest that this is not the case. To confirm this theory, it is suggested that a control sample of heat treated 14YWT at 500 °C for 24 hours should be SANS tested, however this is beyond the scope of this study due to material and experimental availability.

### 4.6. Discussion summary

It is known that the presence of interstitial impurity elements such as nitrogen, carbon, and oxygen can have effects on the corrosion rates in a liquid lithium environment [15], [18], [19] as discussed in the introduction. Whilst the atmospheric oxygen content could be controlled and measured in the glovebox, control and measurement of nitrogen in the atmosphere was beyond the capabilities of the equipment used. Control and measurement of impurity elements within the lithium was also beyond capabilities at the time of this study. This presents opportunities for the control and measurement of interstitial and impurity elements in future studies whilst the present study provides insights into the corrosive effects of commercially available lithium of 99.9% stated purity. Whilst further purification may result in reduced corrosive effects, it is unclear whether this will be feasible in practice on a power plant engineering scale.

Overall, this analysis of corroded fusion-grade material provides insights into the role of nanoparticles using SANS analysis techniques. In addition, the analysis of the materials' microstructure before and after corrosion is used here to give insights into the origins of the pebble-like surface morphology as described by Bell et al. [20] on the corrosion surfaces. Moreover, ODS Y-Ti-O oxide particles appear

to be stable under corrosion and CNA-optimised MX and $M_{23}C_6$ oxide particles are unstable and this is expected due to the thermodynamic instability of ferritic-martensitic steels at temperatures >500 °C [50]. A range of temperatures, exposure time, and interstitial impurity control, along with the developments of thermal convection and forced flowing conditions are recommended to further evaluate the effects of liquid lithium at fusion relevant blanket conditions.

## 5. Conclusions

A particularly attractive engineering method to achieve high tritium breeding in fusion reactors is by using flowing liquid lithium as a breeder and coolant. However, using liquid lithium for this application presents significant technical challenges due to lithium's corrosive properties at the expected operation temperature of the breeder blanket component: at or in excess of 500 °C. This study has investigated three candidate fusion-grade structural material for the blanket: EUROFER ferritic-martensitic steel, CNA steel, and ODS 14YWT steel. The conclusions were as follows:

1) Measurement of sample weight change alone should not be used as a reliable measure of material corrosion performance in the lithium environment in future studies. Microstructural characterisation of corroded samples should also be performed to justify a finding of good resistance to the elevated temperature lithium corrosion environment.
2) Whilst the mass loss and subsequently theorised surface thickness loss of the EUROFER sample during corrosion is not immediately concerning, microstructural characterisation shows that significant and concerning changes have occurred to this material.
3) Significant effects of the corrosion on the CNA sample have been observed; both with respect to its loss of mass and microstructural effects. The loss of key strengthening carbides was observed. This could suggest that this material is unsuitable for application within an elevated temperature environment with direct exposure to liquid lithium.
4) Analysis of the 14YWT ODS steel sample and comparison with the 14WT sample suggests that the presence of relatively thermodynamically stable oxide particles throughout the microstructure may improve the corrosion resistance of the material to the elevated temperature lithium environment.

The microstructural characterisation carried out within this study is unable to definitively state the depth within the sample over which the corrosion has influenced the material microstructure. Whilst outside the scope of this study, it is recommended that the used of focussed ion beam milling or another method of cross sectioning the sample could be used to observe a transverse section of the sample and conclude the maximum depth at which preferential grain boundary attack is observed for instance. Moreover, the study has revealed that the level of understanding on liquid lithium corrosion at high temperatures is low and more investigations across a range of temperatures, flow conditions, and other relevant environmental effects – such as monitoring and control of interstitial impurity elements – is needed to better predict corrosion phenomena.

## 6. Acknowledgements

We are grateful for use of characterisation facilities within the David Cockayne Centre for Electron Microscopy, Department of Materials, University of Oxford, which has benefitted from financial support provided by the Henry Royce Institute (Grant ref EP/R010145/1). CNA material for this work was provided by ORNL and produced by the United States Department of Energy, Office of Fusion Energy Sciences, under contract DE-AC05- 00OR22725 with UT-Battelle, LLC. Funding for this research was part of the United Kingdom Atomic Energy Authority (UKAEA) Small Business Research Initiative (SBRI) Fusion Industry Challenges Cycle 2 Phase 1 programme. We kindly acknowledge Xpress Access on the SANS2D neutron scattering instrument at the ISIS Neutron and Muon source (Experiment number XB2390053).

**References**


[1] M. Abdallah, "An Alternate Design To Liquid Metal Blankets," presented at the 30th IEEE Symposium On Fusion Engineering, Oxford, UK, Jul. 11, 2023.

[2] R. J. Pearson, A. B. Antoniazzi, and W. J. Nuttall, "Tritium supply and use: a key issue for the development of nuclear fusion energy," *Fusion Eng. Des.*, vol. 136, pp. 1140–1148, 2018, doi: 10.1016/j.fusengdes.2018.04.090.

[3] T. E. G. Nicholas *et al.*, "Re-examining the role of nuclear fusion in a renewables-based energy mix," *Energy Policy*, vol. 149, p. 112043, Feb. 2021, doi: 10.1016/j.enpol.2020.112043.

[4] H. Elserafy, "Assessment of DEMO reactors for fusion power utilization," *Evergreen*, vol. 5, no. 4, pp. 18–25, 2018, doi: 10.5109/2174854.

[5] Y. Gohar, S. Majumdar, and D. Smith, "High power density self-cooled lithium–vanadium blanket," *Fusion Eng. Des.*, vol. 49–50, pp. 551–558, Nov. 2000, doi: 10.1016/S0920-3796(00)00279-9.

[6] D. J. M. King *et al.*, "High temperature zirconium alloys for fusion energy," *J. Nucl. Mater.*, vol. 559, p. 153431, 2022, doi: 10.1016/j.jnucmat.2021.153431.

[7] F. Volpe, "Opening Remarks," presented at the FuseNet Fusion Winter School, Fontaine, Fr, 2023.

[8] Fusion Industry Association, "The Global Fusion Industry in 2023."

[9] S. J. Zinkle *et al.*, "Development of next generation tempered and ODS reduced activation ferritic/martensitic steels for fusion energy applications," *Nucl. Fusion*, vol. 57, no. 9, 2017, doi: 10.1088/1741-4326/57/9/092005.

[10] T. P. Davis *et al.*, "Electron microscopy and atom probe tomography of nanoindentation deformation in oxide dispersion strengthened steels," *Mater. Charact.*, vol. 167, p. 110477, Sep. 2020, doi: 10.1016/j.matchar.2020.110477.

[11] C. Cabet, F. Dalle, E. Gaganidze, J. Henry, and H. Tanigawa, "Ferritic-martensitic steels for fission and fusion applications," *J. Nucl. Mater.*, vol. 523, pp. 510–537, Sep. 2019, doi: 10.1016/J.JNUCMAT.2019.05.058.

[12] E. Gaganidze, F. Gillemot, I. Szenthe, M. Gorley, M. Rieth, and E. Diegele, "Development of EUROFER97 database and material property handbook," *Fusion Eng. Des.*, vol. 135, no. February, pp. 9–14, 2018, doi: 10.1016/j.fusengdes.2018.06.027.

[13] L. Tan, Y. Katoh, and L. L. Snead, "Development of castable nanostructured alloys as a new generation RAFM steels," *J. Nucl. Mater.*, vol. 511, pp. 598–604, Dec. 2018, doi: 10.1016/j.jnucmat.2018.05.024.

[14] J. H. DeVan, J. E. Selle, and A. E. Morris, "Review of Lithium Iron-Base Alloy Corrosion Studies," Oak Ridge National Laboratory, 1976.

[15] R. N. Lyon, Ed., "Corrosion of Materials," in *Liquid-Metals Handbook*, 2nd rev., Washington D.C.: U.S. Atomic Energy Commission, 1954, pp. 144–161. doi: 10.1002/9781118737880.ch1.

[16] G. DeVries, "The Corrosion of Metals by Molten Lithium," in *Corrosion by Liquid Metals: Proceedings of the Sessions on Corrosion by Liquid Metals of the 1969 Fall Meeting of the Metallurgical Society of AIME, October 13--16, 1969, Philadelphia, Pennsylvania*, J. E. Draley and J. R. Weeks, Eds., Boston, MA: Springer US, 1970, pp. 251–269. doi: 10.1007/978-1-4684-1845-3_14.

[17] O. K. Chopra and D. L. Smith, "Corrosion of ferrous alloys in a flowing lithium environment," *J. Nucl. Mater.*, vol. 133–134, pp. 861–866, Aug. 1985, doi: 10.1016/0022-3115(85)90275-2.

[18] G. E. Bell, "Thermal convection loop experiments and analysis of mass transport process in Lithium/Fe-12Cr-1MoVW systems," UCLA, 1988.

[19] E. E. Hoffman, "CORROSION OF MATERIALS BY LITHIUM AT ELEVATED TEMPERATURES," University of Tennessee, Oak Ridge, TN, USA, 1959. [Online]. Available: https://www.osti.gov/biblio/4750888

[20] G. E. Bell, M. A. Abdou, and P. F. Tortorelli, "Experimental and analytical investigations of mass transport processes of 12cr-1 movw steel in thermally-convected lithium systems," *Fusion Eng. Des.*, vol. 8, pp. 421–427, Jan. 1989, doi: 10.1016/S0920-3796(89)80142-5.

[21] S. Hammouti *et al.*, "Wetting of liquid lithium on fusion-relevant materials microtextured by femtosecond laser exposure," *J. Nucl. Mater.*, vol. 508, pp. 237–248, Sep. 2018, doi: 10.1016/j.jnucmat.2018.05.051.
[22] R. Kaita *et al.*, "Experiments with liquid metal walls: Status of the lithium tokamak experiment," *Fusion Eng. Des.*, vol. 85, no. 6, pp. 874–881, Nov. 2010, doi: 10.1016/j.fusengdes.2010.04.005.
[23] H. W. Kugel *et al.*, "The effect of lithium surface coatings on plasma performance in the National Spherical Torus Experiment)," *Phys. Plasmas*, vol. 15, no. 5, p. 056118, May 2008, doi: 10.1063/1.2906260.
[24] J. Knaster *et al.*, "Overview of the IFMIF/EVEDA project," *Nucl. Fusion*, vol. 57, no. 10, p. 102016, Oct. 2017, doi: 10.1088/1741-4326/aa6a6a.
[25] A. Harte, M. Preuss, and T. Darby, "Overview and Recommendations on the use of Zr and Ti as Fusion Materials," UKAEA, UK, CD/STEP/00585, 2020.
[26] M. Green, S. Foster, A. Wisbey, A. Cole-Baker, and R. Crutchley, "Review of Titanium Alloy Development Towards Use in a Nuclear Fusion Environment," UKAEA, UK, CD/STEP/00456, 2020.
[27] P. Favuzza *et al.*, "Erosion-corrosion resistance of Reduced Activation Ferritic-Martensitic steels exposed to flowing liquid Lithium," *Fusion Eng. Des.*, vol. 136, pp. 1417–1421, Nov. 2018, doi: 10.1016/j.fusengdes.2018.05.028.
[28] X. Meng *et al.*, "Effect of temperature on the corrosion behaviors of 304 stainless steel in static liquid lithium," *Fusion Eng. Des.*, vol. 128, pp. 75–81, Mar. 2018, doi: 10.1016/J.FUSENGDES.2018.01.049.
[29] D. H. Zhang *et al.*, "Study of the corrosion characteristics of 304 and 316L stainless steel in the static liquid lithium," *J. Nucl. Mater.*, vol. 553, p. 153032, Sep. 2021, doi: 10.1016/j.jnucmat.2021.153032.
[30] C. D. Moynihan, S. Stemmley, B. Moore, R. Trendler, Md. A. Hossain, and D. N. Ruzic, "Characterization of liquid lithium corrosion for fusion reactor materials," *Fusion Eng. Des.*, vol. 199, p. 114102, Feb. 2024, doi: 10.1016/j.fusengdes.2023.114102.
[31] L. M. Giancarli *et al.*, "Status of the ITER TBM Program and overview of its technical objectives," *Fusion Eng. Des.*, vol. 203, p. 114424, Jun. 2024, doi: 10.1016/j.fusengdes.2024.114424.
[32] B. Gómez-Ferrer, C. Dethloff, E. Gaganidze, L. Malerba, C. Hatzoglou, and C. Pareige, "Nano-hardening features in high-dose neutron irradiated Eurofer97 revealed by atom-probe tomography," *J. Nucl. Mater.*, vol. 537, p. 152228, 2020, doi: 10.1016/j.jnucmat.2020.152228.
[33] C. A. Jones, "A micromechanical investigation of proton irradiated oxide dispersion strengthened steels," University of Oxford, 2016.
[34] L. Tan, T. Chen, Y. Yang, L. He, and K. Sridharan, "Development of nanoprecipitates-strengthened advanced ferritic alloys for nuclear reactor applications," Oak Ridge National Laboratory, ORNL/TM--2019/1119, 1526385, Feb. 2019. doi: 10.2172/1526385.
[35] P. Dubuisson, Y. de Carlan, V. Garat, and M. Blat, "ODS Ferritic/martensitic alloys for Sodium Fast Reactor fuel pin cladding," *J. Nucl. Mater.*, vol. 428, no. 1, pp. 6–12, Sep. 2012, doi: 10.1016/j.jnucmat.2011.10.037.
[36] M. Richardson, M. Gorley, Y. Wang, D. Andres, and H. Dawson, "Small punch creep investigation of Eurofer97 and 14Cr oxide dispersion strengthened steel," *Nucl. Mater. Energy*, vol. 29, p. 101067, Dec. 2021, doi: 10.1016/j.nme.2021.101067.
[37] G. R. Odette, "On the status and prospects for nanostructured ferritic alloys for nuclear fission and fusion application with emphasis on the underlying science," *Scr. Mater.*, vol. 143, pp. 142–148, 2018, doi: 10.1016/j.scriptamat.2017.06.021.
[38] M. J. Gorley, "Powder processing of oxide dispersion strengthened alloys for nuclear applications," University of Oxford, 2014.
[39] C. Burrows, "THE IRRADIATION RESISTANCE OF OXIDE DISPERSION STRENGTHENED STEELS," University of Oxford, 2015.
[40] T. P. Davis, "ON NANOSIZED PRECIPITATES IN STEELS FOR ADVANCED NUCLEAR REACTORS," University of Oxford, 2020. Accessed: Apr. 19, 2024. [Online]. Available: https://linkinghub.elsevier.com/retrieve/pii/S0022311521000659

[41] J. Liu *et al.*, “Liquid lithium corrosion of SiC/SiC composites,” *Materialia*, vol. 34, 2024.
[42] S. King, “Small-angle Neutron Scattering,” in *Modern Techniques for Polymer Characterisation*, 1st ed., John Wiley, 1999.
[43] D. R. Lide, *CRC Handbook of Chemistry and Physics*, 81st ed. Boca Raton, FL: CRC Press, 2000.
[44] M. G. Barker and D. J. Wood, “The corrosion of chromium, iron, and stainless steel in liquid sodium,” *J. Common Met.*, vol. 35, no. 2, pp. 315–323, Apr. 1974, doi: 10.1016/0022-5088(74)90243-4.
[45] P. Fernandez, A. M. Lancha, P. Lapena, M. Serrano, and M. Hernandez-Mayoral, “Reduced Activation Ferritic/Martensitic Steel Eurofer´97 as Possible Structural Material for Fusion Devices, Metallurgical Characterization on As-Received Condition and after Simulated Service Conditions,” Ciemat, Madrid, 1048, 2004.
[46] X. Yi, A. Ma, L. Zhang, and Y. Zheng, “Crystallographic anisotropy of corrosion rate and surface faceting of polycrystalline 90Cu-10Ni in acidic NaCl solution,” *Mater. Des.*, vol. 215, p. 110429, Mar. 2022, doi: 10.1016/j.matdes.2022.110429.
[47] F. Balbaud-Célérier, J.-L. Courouau, D. Féron, L. Martinelli, and F. Rouillard, “13 - Corrosion of structural materials by liquid metals used in fusion, fission, and spallation,” in *Nuclear Corrosion*, S. Ritter, Ed., in European Federation of Corrosion (EFC) Series. , Woodhead Publishing, 2020, pp. 437–457. doi: 10.1016/B978-0-12-823719-9.00013-5.
[48] R. L. Klueh, “Penetration of Refractory Metals by Alkali Metals,” in *Corrosion by Liquid Metals*, Springer, 1969, pp. 177–196.
[49] J. R. DiStefano and E. E. Hoffman, “CORROSION MECHANISMS IN REFRACTORY METAL-ALKALI METAL SYSTEMS,” ORNL-3424, 4635104, Sep. 1963. doi: 10.2172/4635104.
[50] R. L. Klueh and A. T. Nelson, “Ferritic/martensitic steels for next-generation reactors,” *J. Nucl. Mater.*, vol. 371, no. 1, pp. 37–52, Sep. 2007, doi: 10.1016/j.jnucmat.2007.05.005.